npj | climate and atmospheric science

Published in partnership with CECCR at King Abdulaziz University

Article

https://doi.org/10.1038/s41612-026-01346-3

Flash flourishing of Northern Hemisphere vegetation and its drivers

Xiangxu Kong[1,2], Jiafu Mao[3] ✉, Haishan Chen[1,2] ✉, Zhenzhong Zeng[4], Yuefeng Hao[3,5], Yaoping Wang[3], Yao Zhang[6], Anping Chen[7], Mingzhou Jin[5], Xiaoying Shi[3] & Forrest M. Hoffman[8]

Rapid surges in vegetation growth—defined by thresholds in growth rate and duration—are critical yet understudied indicators of ecosystem responses to environmental change. Here, we investigate spatiotemporal patterns of such abrupt, short-lived flash flourishing events across the northern extratropical latitudes (NEL) from 2003 to 2022. We find more frequent occurrence of flash flourishing events at high latitudes (≥45° N), where their incidence is 1.6 times higher than at mid-latitudes. Moreover, there is an increasing tendency in frequency, duration, and intensity of flash flourishing events over the past two decades, alongside consistent rises in vegetation indices across onset, post-onset, and entire phases. Model simulations attribute these multiyear increases primarily to elevated atmospheric CO_2, while temperature and radiation predominantly control phase-specific variability, with onset traits strongly predicting subsequent phenological responses. Together, these findings identify the patterns and drivers of NEL flash flourishing and highlight their large-scale impacts on ecosystem dynamics, offering critical insights for model improvement and the assessment of ecological shifts.

Ecosystems are increasingly exhibiting abrupt and short-lived surges in vegetation growth, reflecting complex interactions between environmental drivers and plant physiological responses[1]. Here we refer to these episodes as vegetation "flash flourishing" events: short-duration (weeks) but intense increases in canopy greenness and photosynthetic activity that are superimposed on the regular seasonal cycle. Conceptually, flash flourishing characterizes how quickly vegetation can move from a relatively typical state to an unusually vigorous growth state. Such rapid transitions can temporarily boost carbon uptake and biomass accumulation[2,3], but may also accelerate the depletion of soil water and nutrients and thereby modify subsequent seasonal growth[4], and ecosystem stability[5,6]. Despite this potential importance, flash flourishing remains poorly characterized in its spatiotemporal patterns and mechanistic drivers. Its broad-scale distribution, frequency, and intensity are largely unknown, and the relative contributions of climatic variability, human activities, biotic factors, and legacy effects remain unresolved.

Traditional phenological metrics—such as the start (SOS), peak (POS), and end of the growing season (EOS)—focus on seasonal milestones and average trends[7–9], and therefore overlook transient, high-magnitude growth pulses such as flash flourishing. SOS, POS, and EOS describe when key seasonal transitions occur, whereas flash flourishing describes how fast and how strongly the canopy intensifies over a short time window between these transitions. This blind spot leaves a critical gap in our understanding of how ecosystems respond to rapid environmental forcing. By quantifying the pace of canopy development and senescence, vegetation growth rate (VGR) captures growth intensity and thus complements conventional phenological indicators, revealing how quickly vegetation reacts to both internal physiological cues and external drivers[10–13]. Although our analysis focuses on northern-extratropical ecosystems, a striking illustration of rapid structural growth potential is provided by Moso bamboo (Phyllostachys edulis), a subtropical species that typically grows at a rate of 33–44 cm per day and can surge to 114.5 cm per day under optimal conditions[14]. This example highlights that plants can exhibit extremely rapid increases in height and canopy structure under favorable environmental conditions. Similar, though less extreme, rapid canopy development episodes also occur in temperate and boreal forests and shrublands[15–17], for example during early-season leaf flush

---

[1]State Key Laboratory of Climate System Prediction and Risk Management/Key Laboratory of Meteorological Disaster, Ministry of Education/Collaborative Innovation Center on Forecast and Evaluation of Meteorological Disasters, Nanjing University of Information Science and Technology, Nanjing, China. [2]School of Atmospheric Sciences, Nanjing University of Information Science and Technology, Nanjing, China. [3]Environmental Sciences Division, Oak Ridge National Laboratory, Oak Ridge, TN, USA. [4]School of Environmental Science and Engineering, Southern University of Science and Technology, Shenzhen, China. [5]Institute for a Secure and Sustainable Environment, University of Tennessee, Knoxville, TN, USA. [6]Institute of Carbon Neutrality, Sino-French Institute for Earth System Science, College of Urban and Environmental Sciences, Peking University, Beijing, China. [7]Department of Biology, Colorado State University, Fort Collins, CO, USA. [8]Computational Sciences and Engineering Division, Oak Ridge National Laboratory, Oak Ridge, TN, USA. ✉e-mail: maoj@ornl.gov; haishan@nuist.edu.cn

under warm and moist conditions, and these are captured in our flash flourishing framework. While this rapid height growth is closely tied to species-specific developmental traits, it illustrates the potential for vegetation to undergo short, intense surges in canopy development. Beyond species-specific growth patterns, entire ecosystems can experience short, intense surges in vegetation productivity, highlighting dynamic shifts in ecosystem functioning under rapid environmental changes[1]. These episodes underscore the need for further research to elucidate the mechanisms driving such variability and their implications for ecosystem dynamics.

Building on this conceptual definition, we operationalize flash flourishing as a distinct manifestation of extreme vegetation growth rate characterized by abrupt, short-lived surges in canopy development (Methods, and the schematic representation in Fig. S1b). Specifically, we identify a flash flourishing event when vegetation indices rise from below the 50th percentile to above the 70th percentile within four pentads, with an average increase rate of at least 5% per pentad and a minimum duration of three pentads. We further divide each event into an onset phase, during which percentiles rise rapidly, and a post-onset phase, during which elevated percentiles are maintained and then relax. These rapid growth events emerge from the interplay between internal growth potential and external environmental triggers, and can induce significant ecological transitions over short timeframes.

This study brings a new, rate-based perspective to large-scale vegetation dynamics by explicitly targeting flash flourishing events. Our goals are to (i) quantify the frequency, duration and intensity of flash flourishing across extratropical non-cropland ecosystems north of 30° N, (ii) characterize their onset and post-onset evolution using percentile-transformed vegetation indices, and (iii) identify the environmental drivers underpinning these dynamics and their implications for predictability. Specifically, we address four central questions: (1) Where do vegetation flash flourishing events occur? (2) How are flash flourishing events changing through time? (3) What controls the dynamics of flash flourishing events? (4) Can flash flourishing inform phenological forecasting?

To address these questions, we build an integrated observational-modeling framework that combines multiple satellite vegetation records, climate reanalysis and process-based ecosystem simulations. We use five independent satellite-derived vegetation datasets (SIF and VIs), including continuous solar-induced fluorescence (CSIF), MODIS enhanced vegetation index (EVI) and kernel Normalized Difference Vegetation Index (kNDVI), MODIS leaf area index (LAI), and PKU GIMMS NDVI, which span 2003–2022. To identify key environmental drivers and validate our findings, we combine these observations with climate reanalysis data, factorial simulations from TRENDY v12, and FLUXNET tower observations. We then apply partial least squares regression (PLSR), machine-learning models, structural equation modeling (SEM) and leave-one-out cross-validation (LOOCV) to assess causal relationships and predictive power. This integrated framework enables us to quantify the mechanisms underlying flash flourishing events and evaluate their influence on seasonal vegetation dynamics at continental to hemispheric scales.

Results

Spatial distribution of flash flourishing events

Between 2003 and 2022, flash flourishing events in the northern extratropical latitudes (>30°N; hereafter NEL) occurred in an average of 52.7% of years—rising to 57.5% at ≥45°N but falling to 36.3% at 30°–45° N (Supplementary Fig. S2). Notably, some lower-latitude subregions still exhibit high occurrence rates: for example, southeastern North America (30°–45°N, 60°–95°W) records a 52.5% occurrence rate.

Event frequency, duration, and intensity—defined respectively as the annual number of flash flourishing events per unit area, the total days per event, and the cumulative SIF or VI percentile deficit above the 50th percentile during the event—follow pronounced latitudinal gradients (Fig. 1, Supplementary Figs. S3, S4). Within 10 × 10 grid cells, the total number of events ranges from 1 to 100 events yr^{-1}, peaking at mid–high latitudes (45–60°N) with 0.007 events km^{-2} versus 0.005 events km^{-2} elsewhere (Fig. 1a). Here "events km^{-2}" denotes the total number of events in each 10 × 10 window divided by the land area of that window, so that spatial differences in densities reflect heterogeneity in event occurrence across the underlying grid cells rather than differences in grid-cell size. Likewise, duration and intensity densities reach maxima at 50–60° N (0.008 days km^{-2} and 0.05% km^{-2} at 50–60°N, versus 0.006 days km^{-2} and 0.04% km^{-2} at 30–50°N; Supplementary Fig. S3), where "days km^{-2}" and "% km^{-2}" are defined analogously as the total event days and cumulative intensity in each 10 × 10 window normalized by the land area of that window. Regions with higher frequencies also sustain longer and more intense events—a pattern consistently captured by TRENDY model outputs (Fig. 1b, Supplementary Figs. S3, S4).

When stratified by plant functional type (Supplementary Fig. S5), forests exhibit the highest frequency of flash flourishing events, with an average of 12.7 events per grid cell over the study period, compared to 9.3 in grasslands and 10.7 in shrublands (Supplementary Fig. S6). Forests also experience the longest and most intense events.

We further quantified the average patterns of the original vegetation index—converted to percentiles based on each pixel's multi-year distribution (see Methods)—by temporally averaging values over the onset, post-onset, and entire-event phases of vegetation flash flourishing growth (Fig. 1c, d; Supplementary Figs. S7, S8). Physiologically, these percentile values represent the relative level of canopy photosynthetic activity and greenness within each pixel's own climatology: high percentiles correspond to periods with dense foliage, high chlorophyll content and enhanced photosynthetic capacity, whereas low percentiles indicate relatively sparse canopy and reduced photosynthetic activity. During the post-onset and whole-event stages, both satellite observations and TRENDY models show highest percentiles in eastern Asia and eastern North America, with lower values across central Asia, western North America, and the Arctic. In contrast, onset-phase percentiles peak in northeastern Asia and are comparatively subdued in southeastern Asia and southeastern North America.

Intensifying trends over time

From 2003 to 2022, flash flourishing frequency in NEL increased at 0.009σ yr^{-1} ($p < 0.001$; where σ is the estimated standard deviation), with 73.4% of land (55.5–76.4% among products) trending upward—most markedly in eastern and northern Russia, eastern China, and Canada—while declines were confined to central-western Eurasia and southern North America (Fig. 2a, e; Supplementary Fig. S9a). Duration and intensity rose in parallel (0.01σ yr^{-1}; $p < 0.001$) across 77.4% and 80.4% of the region, respectively, with negative trends limited to 19–23% of the area (Supplementary Fig. S10a, c). Biome breakdowns show shrublands leading in frequency (0.03σ yr^{-1}), duration, and intensity (0.05σ and 0.06σ yr^{-1}) (Supplementary Fig. S11). Taken together, increasing frequency, duration, and intensity indicate that many northern-extratropical ecosystems are spending more time in unusually vigorous growth states and that the magnitude of these rapid-growth episodes is strengthening. This implies greater seasonal carbon uptake and biomass accumulation in the short term, especially in shrubland-dominated regions where duration and intensity increases are strongest. TRENDY GPP and LAI outputs largely reproduce both the magnitude and spatial patterns of these trends (Fig. 2c, e; Supplementary Figs. S10–S12).

Mean vegetation percentiles climbed significantly ($p < 0.001$) during onset (0.0002–0.0003σ yr^{-1}), post-onset (0.0003–0.0004σ yr^{-1}), and whole-event phases (0.0003–0.0004σ yr^{-1}) in both satellite records and TRENDY simulations, corroborated by FLUXNET towers (Fig. 2f; Supplementary Figs. S9b, S12h). Although these slopes appear numerically small because they are expressed in units of the spatial standard deviation, they are spatially coherent across products and accumulate over the two-decade record to detectable shifts towards higher percentiles in many regions, indicating a systematic strengthening of canopy greenness and photosynthetic activity during flash flourishing events. In physiological terms, these upward percentile trends indicate that, during flash flourishing events, canopies are becoming denser and more photosynthetically active relative to their historical seasonal behavior, consistent with

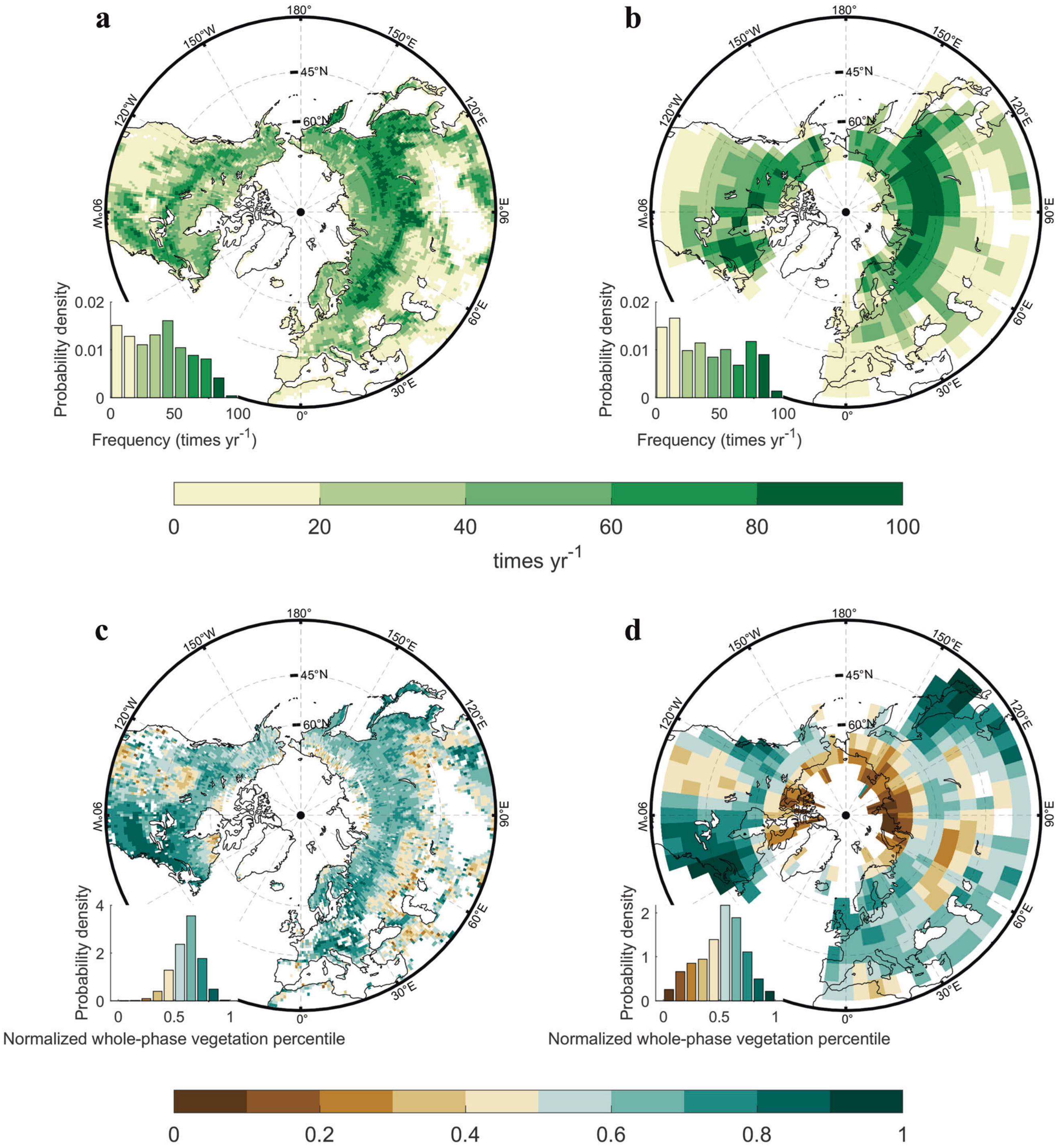

Fig. 1 | Spatial distribution and characteristics of flash flourishing growth events. Ensemble-mean frequency (times yr^{-1}) of flash-flourishing events derived from (**a**) satellite-based observations (CSIF, PKU GIMMS NDVI, MODIS EVI, kNDVI and MODIS LAI) and (**b**) 18 TRENDY v12 S3 scenario GPP model outputs. Frequencies were aggregated over 10 × 10 grid-cell windows, retaining only those windows with ≥10 events. Ensemble-mean whole-phase temporal average vegetation index percentiles based on (**c**) satellite-based indices and (**d**) TRENDY v12 S3 GPP products. Percentiles were computed within 10 × 10 grid-cell windows and scaled to [0, 1] using max-min normalization.

enhanced leaf area, greenness, and canopy carbon assimilation. Conversely, regions with declining percentiles likely experience weaker or less sustained growth surges, potentially reflecting stronger climatic or edaphic constraints on plant functioning. Specifically, approximately 30% of land—principally central-western Asia and southwestern North America—showed declining percentiles in each phase (Fig. 2b; Supplementary Figs. S10e, g, S12e, g), while eastern Asia and northern North America exhibited the strongest positive percentile trends across all datasets (Fig. 2b; Supplementary Figs. S10e, g, S12e, g).

Environmental drivers of event dynamics

Rising atmospheric CO_2 emerges as the dominant driver of positive trends in flash flourishing events across NEL, with CO_2 fertilization accounting for increases in frequency over 84–85% of land (TRENDY GPP: 84.7%; LAI: 84.8%), in duration across 85–90% (GPP: 90.1%; LAI: 85.4%), and in intensity over 81–92% (GPP: 92.2%; LAI: 81.6%) of the region, whereas the ~20% of areas exhibiting negative trends correspond to zones where fewer than nine GPP or six LAI models concur on CO_2, atmosphere, or LULCC effects (Fig. 3a, Supplementary Figs. S13, 14).

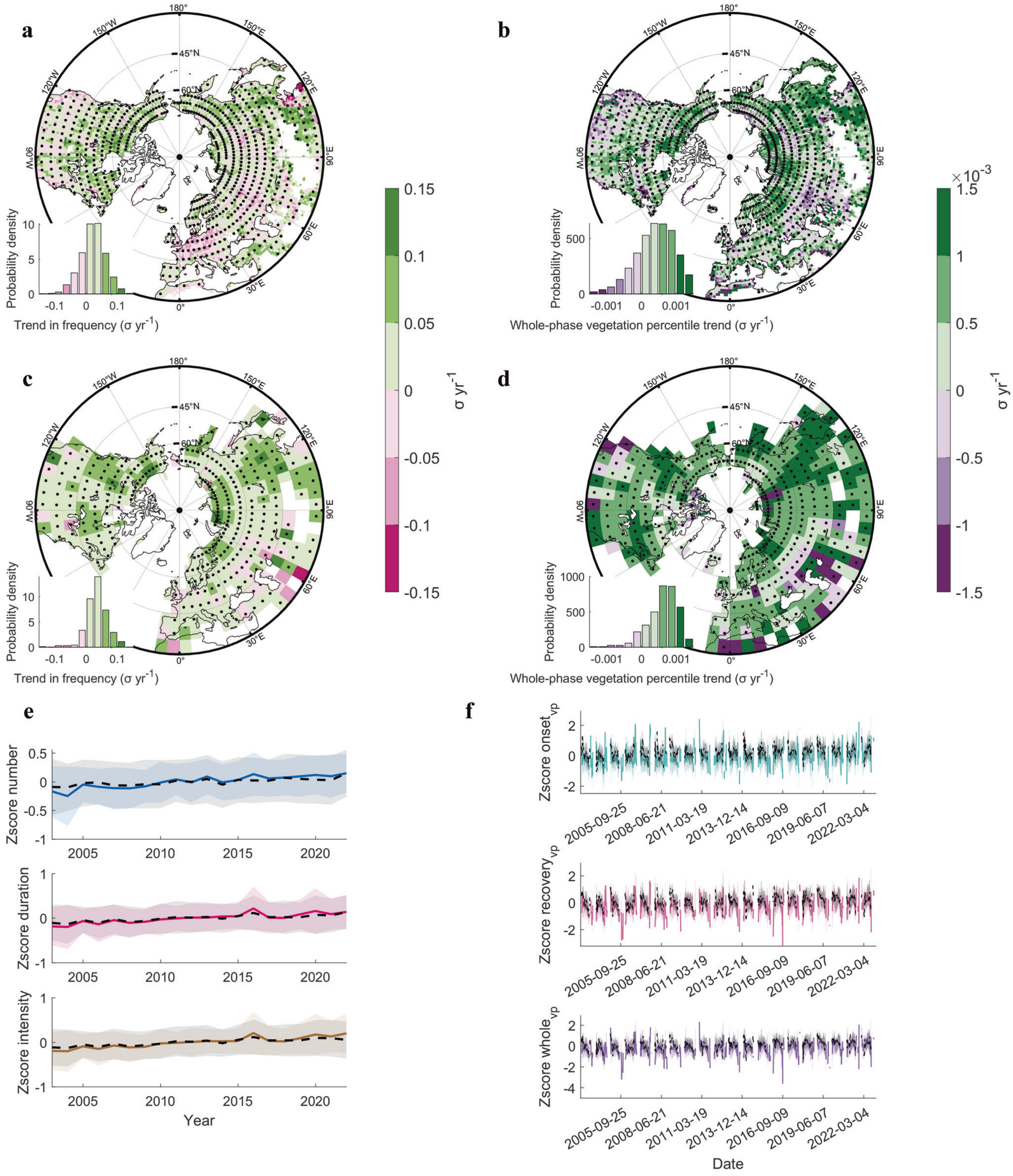

Fig. 2 | Trends in characteristics of flash flourishing growth events. a, **c** Spatial maps of the ensemble-mean trend (*σ* yr^{-1}) in annual event frequency (2003–2022), computed within 10 × 10 grid-cell windows (≥10 events), for (**a**) CSIF, PKU GIMMS NDVI, MODIS EVI, kNDVI, and MODIS LAI datasets, and (**c**) 18 TRENDY v12 S3-scenario GPP products. **b**, **d** As in (**a**) and (**c**), showing trends in mean vegetation percentile at the whole phase (*σ* yr^{-1}) for (**b**) the satellite ensemble and (**d**) the TRENDY S3 GPP ensemble. Stippling indicates grid cells where at least three satellite datasets (**a**, **c**) or nine TRENDY GPP models (**b**, **d**) agree on the sign of the trend. **e** Time series (mean ± 1 s.d.) of Z-score-normalized frequency, duration and intensity of flash-flourishing events (2003–2022), with black dashed lines for satellite products and colored solid lines for TRENDY GPP. **f** As in (**e**), but for Z-score-normalized mean vegetation percentile during onset, post-onset, and whole phases (onset$_{vp}$, post-onset$_{vp}$, whole$_{vp}$).

Across onset, post-onset and whole-event phases, CO_2 fertilization drives positive percentile trends over 35.7–42.0% of land (onset: GPP 42.0%, LAI 35.7%; post-onset: GPP 37.5%, LAI 36.0%; whole: GPP 40.2%, LAI 38.1%), while atmospheric change induces negative trends over 18.9-30.1% (onset: GPP 27.3%, LAI 18.9%; post-onset: GPP 30.1%, LAI 22.1%; whole: GPP 29.7%, LAI 19.4%), yielding CO_2-driven increases concentrated in eastern Asia and northern North America and atmosphere-driven declines in central-

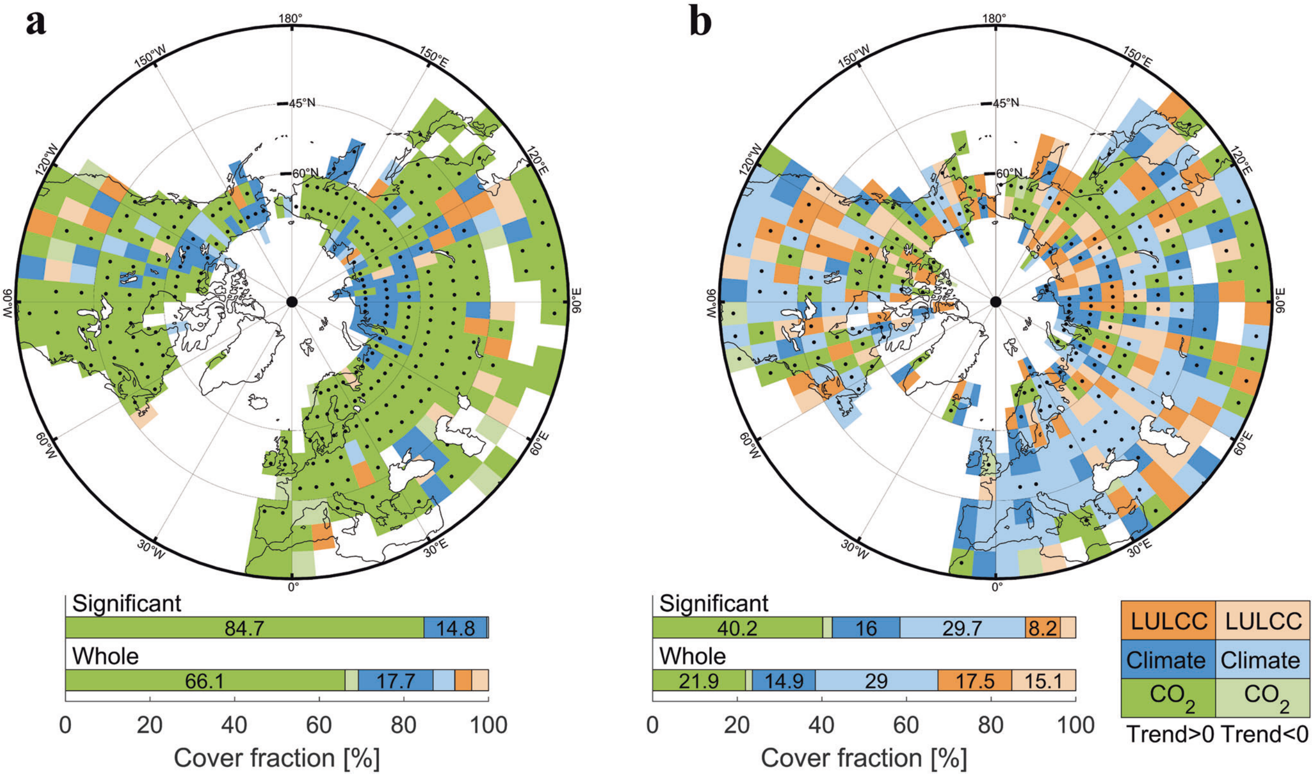

Fig. 3 | Spatial patterns of the dominant drivers of trends in vegetation flash flourishing growth. **a** Ensemble-mean map of the dominant process driving trends in flash flourishing event frequency per 10 × 10 grid cell over 2003–2022. **b** Ensemble-mean map of the dominant process driving trends in whole-phase percentiles of flash flourishing growth per 10 × 10 grid cell over 2003–2022. Dominance is assigned to the process (CO_2 fertilization, atmospheric change or land-use and land-cover change (LULCC)) that produces the largest absolute trend magnitude in each cell. Event frequency is defined as the total number of flash flourishing events per cell. Maps show ensemble means across 18 GPP datasets within the TRENDY model suite under all scenarios. Black dots mark grid cells where at least nine datasets agree on the direction of the trend.

western Asia and southwestern North America (Fig. 3b, Supplementary Figs. S13, S14).

From 2003 to 2022, nearly all flash flourishing growth events in NEL occurred within the VGU-VSS category, beginning during the vegetation green-up period (VGU; from SOS to POS) and ending during the vegetation senescence period (VSS; from POS to EOS) (Supplementary Fig. S15), a timing also seen in TRENDY simulations (Supplementary Fig. S26). By construction, flash flourishing events are defined between SOS and EOS, and the date of POS is almost always embedded within the event window, typically during the post-onset phase (Supplementary Fig. S23). Thus, when we classify events as occurring between VGU and VSS, POS is inherently included within this interval. A PLSR model explains most variability in SIF and VI percentiles across onset ($R^2 = 0.7 \pm 0.1$), post-onset ($R^2 = 0.6 \pm 0.1$) and whole-event phases ($R^2 = 0.7 \pm 0.1$; Supplementary Fig. S16). Across the full event, radiation (RAD) and temperature (TMP) together account for 65.0% of the explained variability—RAD dominating north of 50° N, TMP below—while during onset TMP drives 77.7% of variability and during post-onset RAD drives 51.7%, suggesting warmth accelerates initiation but high radiation may impede post-onset (Fig. 4a, c, e; Supplementary Fig. S17).

A Deep Forest model captures 20–40% of phase-specific variance in CSIF, EVI, LAI, kNDVI, and NDVI ($R^2 = 0.2$–0.4; Supplementary Figs. S18–S22), consistently identifying TMP as the principal positive onset driver and RAD as the dominant negative post-onset driver. TRENDY models mirror the dominance of TMP in onset (GPP 81.9%; LAI 74.6%) and RAD in post-onset (GPP 91.4%; LAI 72%) but fail to replicate the observed high-latitude RAD inhibition and low-latitude TMP enhancement over the whole period (Fig. 4b, d, f; Supplementary Figs. S27–S29).

Predicting phenological shifts

The flash flourishing onset characteristics offer strong, advanced predictions of peak greenness, POS and EOS across NEL. In 99.4% of the domain, POS occurs after the flash flourishing growth onset–end period (Supplementary Fig. S23), with lags of up to 30 days in northeastern Europe and eastern North America (Supplementary Fig. S24a). A process-based model driven solely by onset metrics reproduces spatial patterns with mean predictabilities of 67.9% for peak greenness ($r = 0.15$, $p < 0.001$; RMSE = 0.13) (Fig. 5a; Supplementary Figs. S30a–b, S31a), and 92.9% for POS ($r = 0.62$, $p < 0.001$; RMSE = 21.8 days) (Fig. 5c; Supplementary Figs. S20c–d, S31b), though it underestimates peak values in Central Asia and southeastern North America and overestimates POS in parts of Europe and North America. Likewise, EOS can be forecast ~170 days in advance (Supplementary Fig. S24b), yielding predictability of 93.9% ($r = 0.52$, $p < 0.001$; RMSE = 35.4 days) and correctly capturing early EOS in Asia and northern North America and delayed EOS in Europe and southern North America (Fig. 5e; Supplementary Figs. S30e, f, S31c). Using the same predictive approach, the TRENDY models also effectively capture the spatial patterns of phenological metrics (Supplementary Figs. S36–S39).

For peak greenness, leave-one-out cross validation (LOOCV) shows that the SIF and VIs value at onset end ($\mathrm{Index}_{\mathrm{OE}}$) contributes 68.8%, the average SIF and VIs during the onset period ($\mathrm{Index}_{\mathrm{avg}}$) 23.5%, and the SIF and VIs at onset beginning ($\mathrm{Index}_{\mathrm{OB}}$) 7.7% (Supplementary Fig. S25a). In predicting POS, the onset start date ($\mathrm{Date}_{\mathrm{OB}}$) accounts for 76.9%, the end date ($\mathrm{Date}_{\mathrm{OE}}$) 22.0%, and the duration between them ($\mathrm{ONS}_{\mathrm{duration}}$) 1.1% (Supplementary Fig. S25b). Similarly, for EOS forecasting, $\mathrm{Date}_{\mathrm{OB}}$ remains the primary driver at 57.5%, $\mathrm{Date}_{\mathrm{OE}}$ contributes 40.5%, and $\mathrm{ONS}_{\mathrm{duration}}$ 2.0% (Supplementary Fig. S25c). SEM models further demonstrate that direct onset effects (|path coefficients|> 0.2) consistently exceed indirect,

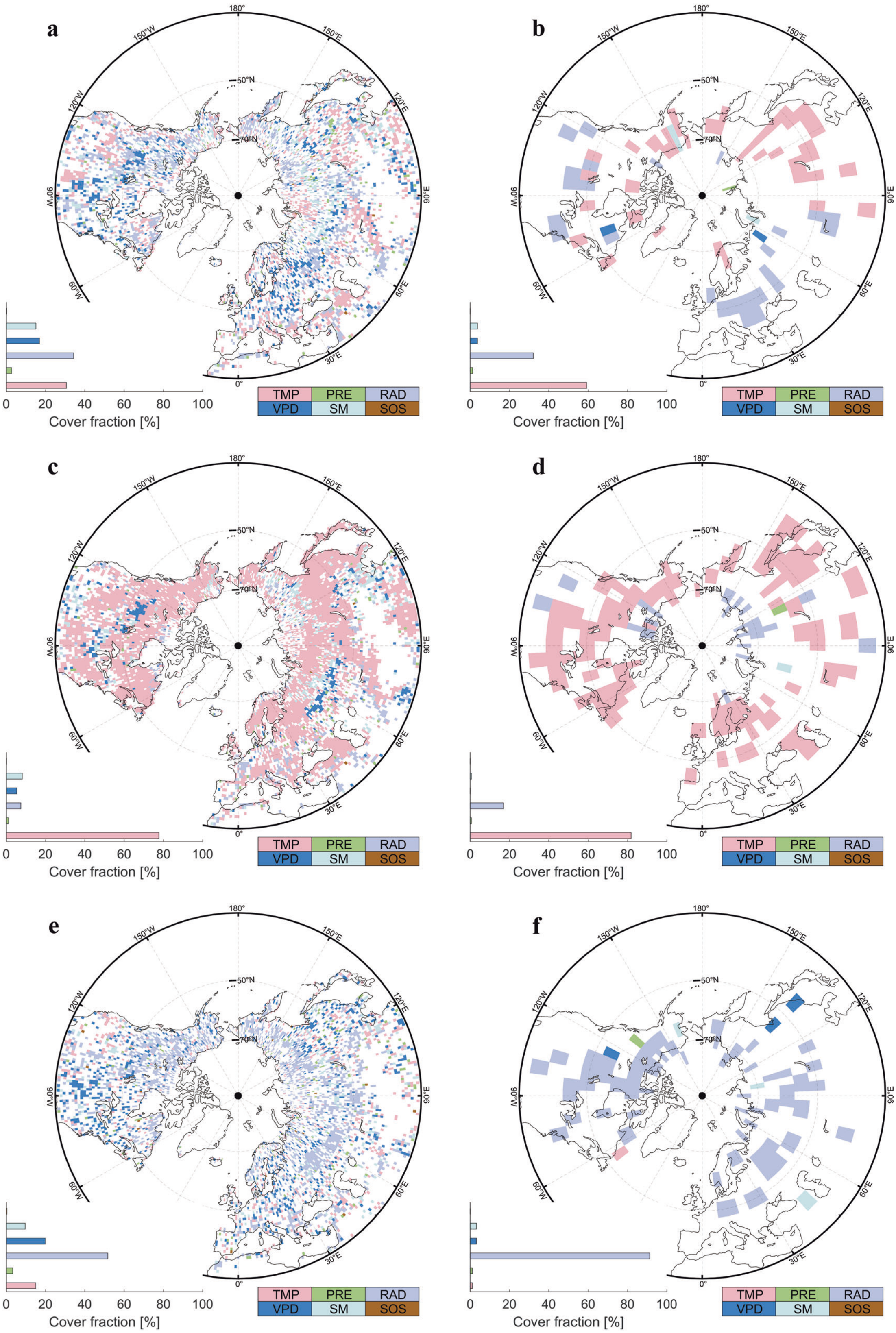

Fig. 4 | Spatial patterns of the dominant drivers of vegetation percentile variability during flash flourishing growth. Panels **a**, **c** and **e** show results for the entire growth period, the onset phase and the post-onset phase, respectively, derived from five independent vegetation datasets (CSIF, PKU GIMMS NDVI, MODIS EVI, MODIS NDVI and MODIS LAI). Only drivers consistently identified in at least three datasets are mapped. Panels **b**, **d** and **f** present the equivalent analysis for gross primary productivity (GPP) using 18 model outputs from the TRENDY Phase S3 scenario, with only drivers recurring in at least nine simulations displayed. All maps were computed using a 10 × 10-grid spatial window to ensure robust statistical estimates.

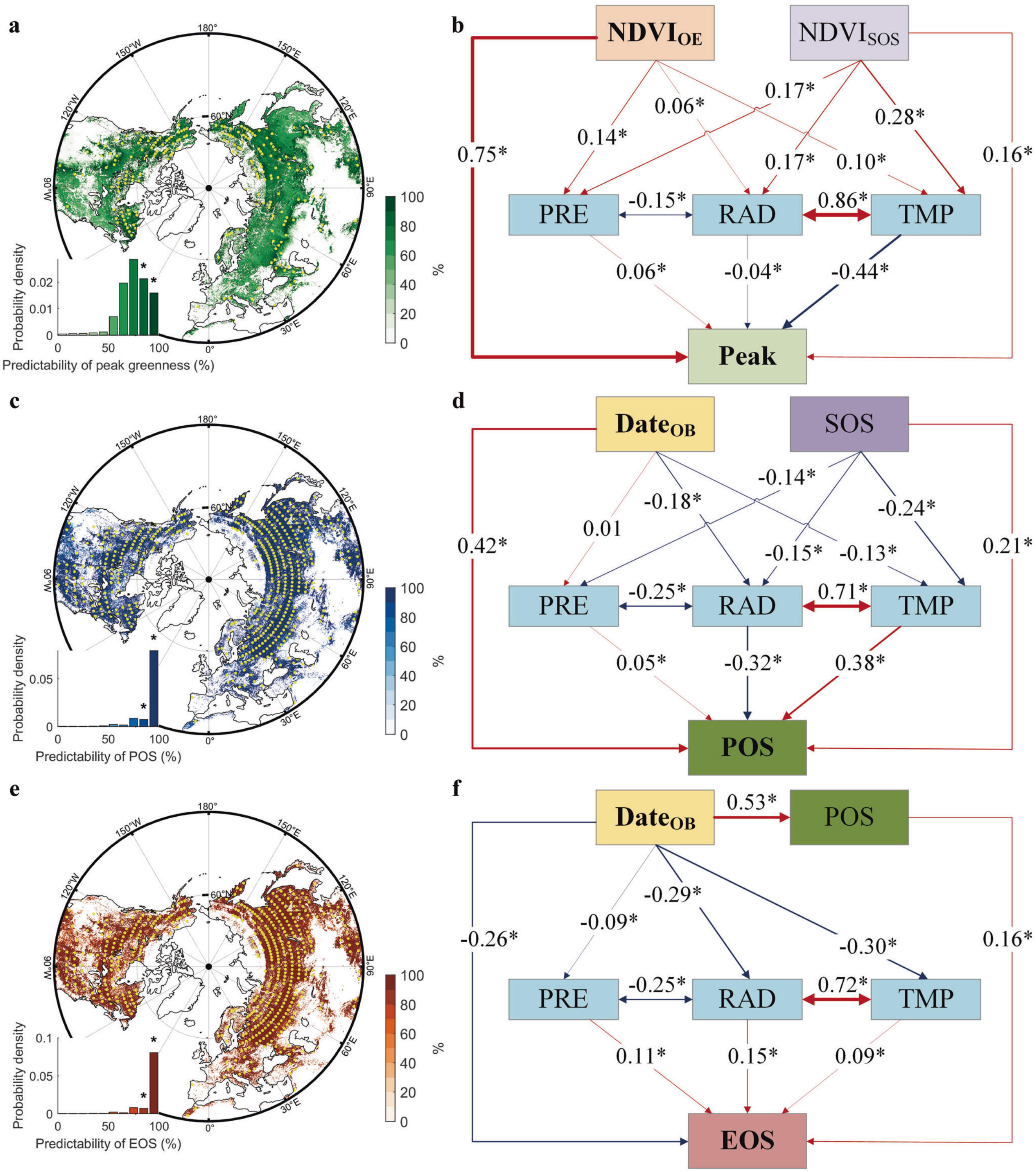

Fig. 5 | Predictions of peak greenness, POS and EOS across NEL. Spatial patterns of the predictability of peak greenness (**a**), POS (**c**) and EOS (**e**), shown as the ensemble mean of CSIF, PKU GIMMS NDVI, MODIS EVI, kNDVI and MODIS LAI. Path diagrams for peak greenness (**b**), POS (**d**) and EOS (**f**), based on the PKU GIMMS NDVI dataset. Standardized path coefficients are indicated beside each arrow, with asterisks denoting significance ($*p < 0.001$). Model-level p-values for overall SEM fit are reported in Supplementary Table S5. Arrow color indicates coefficient sign (blue, negative; red, positive) and arrow width is scaled to coefficient magnitude. Yellow dots indicate grid cells with predictability greater than 80%. An asterisk (*) above the bars indicates bins with predictability greater than 80%.

atmosphere-mediated pathways (|path coefficients|< 0.16) across all five satellite datasets (Fig. 5b, d, f; Supplementary Figs. S32–S35).

Discussion

Our study reveals that vegetation flash flourishing events characterized by rapid and transient bursts of canopy expansion are intensifying across NEL, with 73.4%, 77.4%, and 80.4% of the study area showing increasing trends in frequency, duration, and intensity from 2003 to 2022, while vegetation percentiles during onset, post-onset, and whole-event phases also rose consistently—exhibiting highly significant ($p < 0.001$) positive trends (onset: 0.0002σ yr^{-1}; post-onset: 0.0003σ yr^{-1}; whole: 0.0003σ yr^{-1}). These events, most prevalent in high-latitude ecosystems, are primarily driven by rising atmospheric CO_2, with TMP and RAD shaping regional variability. Notably, onset-phase characteristics strongly predict phenological milestones, offering valuable guidance for ecological forecasting.

Flash flourishing events, almost exclusively occur during the VGU-VSS transition with an occurrence rate nearing 100% (Supplementary Fig. S15). In the early growing season, rising temperatures and ample soil moisture create optimal conditions for accelerated biomass accumulation[18,19]. However, this surge often exhausts soil water and nutrients prematurely, inducing moisture stress and nutrient limitation later in the season[20,21]. As resources dwindle, plants reallocate carbon belowground—enhancing root and stem growth at the expense of leaf production[22]—thereby reducing the frequency of flash-flourishing events. Finally, the onset of senescence, with its attendant decline in photosynthetic and carbon-assimilation capacity, further curtails rapid growth in the season's latter stages[1].

In light of our long-term trend analyses, TRENDY models consistently implicate CO_2 fertilization as the principal driver of the observed intensification in different metrics of flash flourishing events across NEL (Fig. 3). Elevated atmospheric CO_2 enhances photosynthetic capacity and water-use efficiency, thereby promoting more frequent and vigorous canopy growth surges under optimal moisture conditions[23,24], in alignment with previous findings from "greening" studies[23,24]. At the same time, LULCC modulates these trends by altering carbon and hydrological cycles, which can either amplify or locally attenuate flash flourishing responses[25,26]. Moreover, rising temperatures have extended growing seasons and accelerated phenological transitions, while changes in surface radiation regimes—driven by aerosol and cloud feedbacks—modulate light availability, both of which contribute to the heightened events[27]. The synergistic interplay among CO_2 fertilization, LULCC, and atmospheric conditions underscores the long-term mechanistic drivers underlying our findings.

Roughly 30% of the study area—particularly central-western Asia and southwestern North America—shows declining flash flourishing events frequency, duration, and intensity, yet TRENDY models[28] disagree on the drivers: fewer than nine models for GPP and six for LAI concur on the roles of CO_2, atmosphere, or LULCC (Fig. 3a, Supplementary Figs. S13, S14). These divergences likely stem from an overestimated CO_2-fertilization effect under aridity and nutrient scarcity[29,30], and from simplified physiological schemes that, while capturing broad flash flourishing patterns (e.g., strong temperature control at onset), fail regionally (Fig. 4, Supplementary Fig. S28). As shown in Fig. 4a, b, models underplay RAD's photo inhibitory and energy-balance stresses[31] at high latitudes, while they understate TMP's nonlinear growth benefits[32] at low latitudes. Such biases underscore the need for enhanced process-level detail in state-of-the-art ecosystem models.

The variability of flash flourishing events during the VGU-VSS transition in the NEL region reflects both regional climatic gradients and stage-specific vegetation responses (Fig. 4). North of 50°N, prolonged summer daylight increases radiation loads, causing photoinhibition and higher evaporative demand that stress plants[33,34]. South of 50°N—dominated by grasslands (Supplementary Fig. S5)—vegetation remains temperature-limited, so elevated TMP enhances metabolic activity and growth[35]. At event onset, rising TMP accelerates enzymatic reactions and cell division, driving rapid early growth[36]. During post-onset, excessive RAD continues to impose thermal and oxidative stress, hindering full vegetation rebound[37]. These patterns demonstrate that flash flourishing dynamics arise from a balance between beneficial warming and potentially deleterious radiation across space and developmental stages.

Previous research has demonstrated robust correlations between SOS and POS across diverse ecosystems, establishing SOS as a reliable predictor of POS timing[38]. Additionally, studies have shown that regions with higher SIF or VIs at SOS tend to exhibit greater peak SIF or VIs values later in the season[39,40]. Building upon these findings, our study moves beyond traditional phenological metrics by using characteristics derived from the onset phase of flash flourishing growth events to predict both peak greenness and POS (Fig. 5). SEM model consistently reveals that onset-phase features exert a stronger influence on peak greenness and POS than conventional phenological indicators across all datasets (Fig. 5 and Supplementary Figs. S32–S35). Mechanistically, a stronger and more rapid onset of flash flourishing reflects an early-season build-up of leaf area, chlorophyll content, and photosynthetic capacity under favorable temperature, moisture, and radiation conditions. Once this structural and physiological "head start" is established, it largely constrains the subsequent seasonal trajectory: canopies that enter the season quickly and vigorously tend to reach higher peak greenness and, in some regions, an earlier POS, whereas weaker or delayed onset signals limited growth potential or stronger environmental constraints and is associated with lower peak greenness and a later, flattened seasonal maximum. Supporting this, prediction models using only onset-phase features achieved the lowest RMSE values—0.13 for peak greenness and 21.8 days for POS. In contrast, incorporating both onset features and phenological factors (i.e., SIF or VIs at SOS and SOS) led to higher RMSEs—by 0.04 for peak greenness (0.17) and 7.8 days for POS (29.6)—further emphasizing the superior predictive power of onset-phase characteristics.

Onset-phase metrics alone predict EOS with an RMSE of 35.4 days—surpassing both post-onset phase features (RMSE = 36.1 days) and their combination (RMSE = 41.1 days). This finding highlights the onset phase's pivotal role in seasonal vegetation dynamics, informing not only peak productivity (greenness and POS) but also EOS timing. By capturing the rapid acceleration of photosynthetic activity and growth triggered by early warming, onset characteristics effectively integrate the key climatic drivers that guide subsequent development[41–43]. Furthermore, a conserved carbon-allocation strategy—where vegetation maintains a stable ratio of investment between green-up and senescence despite interannual atmospheric changes[38]—may propagate onset-phase variability throughout the growing season, ultimately modulating senescence phenology. Thus, onset-stage traits emerge as robust predictors of both peak performance and EOS, underscoring the decisive influence of early-season conditions on the entire seasonal trajectory.

The congruence between the spatial pattern of EOS predictability (Fig. 5e) and the percentage of years exhibiting vegetation flash flourishing growth (2003–2022; Supplementary Fig. S2) indicates that areas experiencing rapid green-up pulses also exhibit stronger coupling between onset-phase dynamics and autumn senescence timing. This pattern is likely driven by cumulative spring thermal accumulation, which accelerates photosynthetic activity and sets developmental trajectories that constrain senescence onset[10,11,44]. Eastern North America and central-eastern Asia, where flash-flourishing events are most frequent, demonstrate the highest EOS forecast skill, underscoring a mechanistic linkage between onset-phase dynamics and senescence initiation[45,46]. Integrating onset-phase metrics into ecosystem models may therefore improve predictions of growing-season length and associated carbon fluxes under future warming scenarios[47–49]. However, this study does not consider how the early-season characteristics of rapid vegetation growth, via physiological pathways such as cytokinin activity[50], shape subsequent phenological transitions, owing to a lack of direct observations. It also overlooks whether extreme climatic events (e.g., drought or heatwaves) might weaken or strengthen the linkage between onset-phase dynamics and later phenological stages[38]. Together, these methodological gaps and data shortages highlight the urgent need for coordinated, long-term field experiments and high-frequency monitoring to untangle how plant physiological processes and environmental stressors jointly drive the full seasonal cycle of vegetation growth.

In summary, our study reveals the rapid intensification of vegetation flash flourishing events across NEL, driven by rising CO_2 and shaped by TMP and RAD. These surges, most frequent in high-latitude ecosystems, predict key seasonal milestones, offering a new lens for ecological forecasting. This framework highlights ecosystem sensitivity to environmental change, with implications for phenology prediction. Future research should explore physiological triggers through field studies, assess extreme environment impacts, and integrate these dynamics into Earth system models to enhance predictions. By enabling early warning systems, flash flourishing can inform environmental adaptation strategies, from forest management to policy. This work positions rapid growth surges as critical indicators of ecological change, paving the way for transformative approaches to managing ecosystems in a changing environment.

Methods

Definition of vegetation flash flourishing growth events

Daily continuous SIF and VIs were derived using three commonly employed methods to fit the raw dataset: harmonic analysis (HANTS), a sixth-order polynomial function (Polyfit), and the cubic-spline method (Spline)[11,51]. Subsequently, the mean SIF and VIs for pentad intervals (5 days) were computed for each fitted daily curve. The pentad mean SIF and VIs of the three fitted curves were then converted to percentiles based on all values from 2003 to 2022 for each grid point, respectively.

Rather than applying de-seasonalization, percentiles were calculated from the full annual distribution (2003–2022) at each grid cell. This approach retains phenological context, allowing flash flourishing events to be interpreted as unusually rapid greening relative to typical seasonal dynamics. CSIF provides a proxy for canopy-level photosynthetic emission, while EVI, NDVI, and kNDVI capture foliage greenness, chlorophyll content, and the fraction of absorbed photosynthetically active radiation, and LAI reflects the amount of leaf area in the canopy. After transforming each time series to percentiles, values close to 100% (or the upper part of the distribution) therefore correspond to periods when the canopy is relatively dense and photosynthetically active compared to its own climatology, whereas values close to 0% represent relatively sparse, less active canopy conditions. In other words, the percentile scale preserves the underlying physiological information (leaf area, greenness and photosynthetic activity), but expresses it as a dimensionless measure of how unusual the current state is for that pixel.

Building upon the methodology established in a previous study on "flash drought" events[52], we incorporated criteria for the rapid increase rate of SIF- and VI-based percentiles and the duration of the flash flourishing growth in this investigation. Specifically, a flash flourishing growth event was defined by the pentad mean SIF or VIs percentile increasing from below the 50th percentile to the 70th percentile, with an average increase rate of no less than 5% per pentad.

Let $X_i(t)$ denote the pentad-mean value of a given vegetation index (SIF or VI) at grid cell i and pentad t (2003–2022), and let $P_i(t)$ denote its percentile (0–100) with respect to the multi-year distribution at that grid cell. A flash flourishing event at grid cell i is defined as a contiguous set of pentads $\mathcal{T}_e = \{t_0, \ldots, t_1\}$ satisfying (1) $P_i(t_0) < 50$, (2) $P_i(t_1) \geq 70$, (3) $\frac{P_i(t_1)-P_i(t_0)}{t_1-t_0} \geq 5$ percentile points per pentad, and (4) $|\mathcal{T}_e| \geq 3$ pentads.

This study adopts the 50–70th percentile thresholds for defining flash flourishing events. Initiating an event from below the climatological median ($P < 50$) ensures that we only capture transitions from a relatively suppressed to an enhanced canopy state, rather than simply tracking acceleration within an already high-growth regime. Requiring the percentile to reach at least the 70th percentile within at most four pentads imposes an average intensification rate of at least 5 percentile points per pentad, which is consistent with the notion of a rapid, "flash-like" event. We acknowledge that early stages of seasonal green-up can also exhibit relatively fast growth; such episodes are included in our framework when they exhibit a rapid transition from below-median to upper-quantile conditions, but more gradual early-season increases that remain close to the climatological median are intentionally excluded.

Our use of percentile-based thresholds and rate constraints is conceptually inspired by flash drought definitions, which distinguish flash events from gradual evolution using rapid changes in soil moisture percentiles over a limited time window[52]. In typical flash drought formulations, a rapid-onset event is identified when soil moisture percentiles drop from at or above the 40th percentile to below the 20th percentile within approximately four pentads, corresponding to a mean decline rate of at least 5 percentile points per pentad. Here we adopt the same idea of a rate-limited percentile transition, but adapt it to vegetation percentiles and canopy development: flash flourishing events are defined as increases from below the 50th percentile to at least the 70th percentile within at most four pentads, with a minimum average increase rate of 5 percentile points per pentad. These thresholds are therefore conceptually related to, but not a direct transfer of, soil-moisture criteria used in flash drought studies. By contrast, higher percentile ranges such as 60–80th would, by construction, omit the critical suppressed-baseline phase and typically require more than four pentads to traverse an equivalent percentile range, thereby violating both the duration and rate constraints that are central to flash-event dynamics. Conversely, substantially lower thresholds would blur the distinction between rapid, flash-like intensification and gradual seasonal growth, because more modest and slowly evolving increases would also satisfy the criteria.

The flash flourishing growth period was divided into two distinct phases: an onset phase and a post-onset phase. The onset phase begins when SIF or VIs percentile exceeds the 50th percentile and is considered complete when either SIF or VIs percentile starts to decline or the average rate of increase falls below 5% (see schematic representation in Supplementary Fig. S1b). The post-onset phase is defined as the interval from the end of the onset phase until the elevated SIF or VIs percentile returns to below 70th (see schematic representation in Supplementary Fig. S1b). Moreover, flash flourishing growth events were required to last for at least 3 pentads (15 days).

This definition combines several elements that are designed to isolate ecologically meaningful, flash-like growth surges. The percentile thresholds are defined relative to each pixel's own multi-year distribution and therefore capture statistically significant departures from its typical canopy state, rather than absolute values that vary across biomes. The rate criterion (an average increase of at least 5 percentile points per pentad) ensures a genuinely rapid transition, distinguishing flash flourishing events from gradual seasonal greening. The division into onset and post-onset phases allows us to separately analyze the climatic and physiological controls on the initiation of rapid growth and on the maintenance and relaxation of the elevated canopy state. The minimum duration requirement of three pentads (~15 days) filters out short-lived anomalies that are more likely to reflect noise or retrieval artefacts and are less likely to correspond to ecologically meaningful changes in canopy structure and function. Finally, we restrict the analysis to the growing season (between SOS and EOS), because outside this period vegetation indices are low and noisy and small fluctuations do not represent true flash flourishing. Together, these choices provide a robust framework for investigating extreme vegetation dynamics and their environmental drivers. Furthermore, the intensity $I_e(i)$ of a flash flourishing event at grid cell i is defined as the accumulated percentile excess above the 50th percentile threshold:

$$I_e(i) = \sum_{t \in \mathcal{T}_e} \big(P_i(t) - 50\big) \tag{1}$$

so that longer events and events with higher percentiles contribute larger intensities.

To describe spatial patterns of flash flourishing occurrence and strength, events were first detected at the native 1/12° land grid. For each grid cell, we computed the number of events, total event days and cumulative intensity over 2003–2022. These quantities were then aggregated within 10×10 pixel windows (containing the underlying 1/12° land grid cells) to obtain robust local statistics. For each window, we summed event counts, event days and cumulative intensity across all land cells and divided by the land area of that window, yielding area-normalized densities in units of events km^{-2}, days km^{-2} and % km^{-2}. Thus, spatial variations in the reported densities reflect heterogeneity in flash flourishing occurrence and strength across grid cells, rather than differences in nominal grid-cell size.

Max-min normalization

For each variable x, the minimum and maximum values are determined from a representative calibration dataset (e.g., the NEL whole-phase average vegetation percentile) to capture its full dynamic range. Normalized value x' is computed as:

$$x' = \frac{x - \min(x)}{\max(x) - \min(x)} \tag{2}$$

mapping x' to [0,1] and ensuring comparability across sensors and models[53].

Attribution of trends in vegetation flash flourishing growth

We employed TRENDY models to isolate the individual contributions of CO₂, atmosphere, and LULCC to vegetation flash flourishing growth. By comparing differences among the scenarios (S1–S0, S2–S1, and S3–S2), we quantified the distinct impacts of each forcing factor. After obtaining both single-forcing and combined-forcing (S3) datasets, we normalized the long-term time series by converting them to Z-scores, defined as

$$Z = \frac{G - \mu}{\sigma} \tag{3}$$

in which Z represents the normalized score, G denotes metrics of flash flourishing growth (including the frequency, duration, and intensity of flash flourishing growth events and the onset, post-onset, and overall period of SIF or VIs percentiles during flash flourishing growth), and μ and σ are the multi-year mean and standard deviation of G, respectively, calculated over the overlapping period from 2003 to 2022. We then derived the trend for each forcing scenario by applying linear regression to the normalized data.

Algorithms of vegetation phenology

For the HANTS and Polyfit methods, the dates corresponding to the maximum and minimum values of the first-order derivative of the fitted daily curves were identified as the SOS and EOS respectively[51,54,55]. The SOS and EOS for the Spline method were determined using the mid-point approach[51,56]. The POS was defined as the date with the peak value in each fitted seasonal curve. Considering that plants typically do not grow below 0 °C[55], we additionally utilized the thermal growing season, which is characterized by daily TMP above 0 °C, to constrain the SOS and EOS and mitigate the risk of spurious phenology based on the TMP product of the CRU JRA. The SOS, POS, and EOS were determined as the average values obtained from applying each of the three methods individually, ensuring a comprehensive representation of phenology in this study.

Coincidence analysis for phenology and flash flourishing growth occurrence timing

We analyzed the relationship between vegetation phenology and the timing of flash flourishing growth. For each grid cell and year, the SOS, POS, and EOS were derived from the smoothed vegetation index time series as described above. We then defined the vegetation green-up period (VGU) as the interval from SOS to POS, and the vegetation senescence period (VSS) as the interval from POS to EOS (see the schematic representation in Supplementary Fig. S1b).

Flash flourishing events were classified according to the positions of their onset and end dates relative to these phenological phases. For each event, we denote by the pentad of onset beginning (t_{OB}) and by the pentad when the event ends (t_{end}). Events for which both t_{OB} and t_{end} lie between SOS and POS were assigned to the VGU-VGU class. Events with t_{OB} between SOS and POS and t_{end} between POS and EOS were assigned to the VGU-VSS class. Events for which both t_{OB} and t_{end} lie between POS and EOS were assigned to the VSS-VSS class. Events whose onset or end fell outside the SOS-EOS interval were excluded from this phenological timing analysis. We then calculated, for each grid cell and biome, the relative frequencies of events in each timing class to quantify how often flash flourishing growth is confined to green-up, spans green-up and senescence, or is confined to senescence.

Analysis of the factors influencing flash flourishing growth variability

To assess the variability in the onset, post-onset, and overall period of SIF or VIs percentiles during flash flourishing growth, long-term trends were removed from these indices. Partial Least Squares Regression (PLSR) was then used to address potential collinearity among the environmental factors. PLSR mitigates multicollinearity by projecting highly correlated independent variables onto a set of orthogonal latent variables that maximize the covariance between predictors and the response variable, thereby reducing the impact of collinearity on regression outcomes[57]. Each regression model was fitted across all spatial grid cells and events to ensure consistent analysis over the study domain. The performance of the PLSR model was evaluated using the R-squared (R^2) score[58].

This study analyzed flash flourishing growth using 21 factors, with long-term trends removed. These factors included both current climatic variables (average pentad values at the onset of flash flourishing growth) and lagged variables, ranging from the prior pentad to three pentads (15 days). For example, TMP_lag1 refers to the mean TMP of the prior 5-day period before the onset or post-onset of the flash flourishing growth event. The variables considered included TMP, PRE, RAD, VPD, SM, and phenological indicators such as SOS. The dominant factor was identified as the one with the highest absolute regression coefficient. To account for scale differences among variables, all factors were Z-score normalized, thereby minimizing potential scaling-related errors[59].

In addition, we employed machine learning models to further validate the dominant factors influencing variability. To mitigate the risk of overfitting inherent in deep learning models, we used the Deep Forest model. This model eliminates the need for fine-tuning hyperparameters and autonomously determines the optimal model complexity based on input data size, ensuring robust generalizability[60,61]. The datasets were divided into training (80%) and test (20%) sets. The performance of the Deep Forest model was also assessed using R^2 on the test set. To further investigate the contribution of each factor, we applied the SHapley Additive exPlanations (SHAP) method[62], which elucidates how variability in the onset, post-onset, and overall period of SIF or VIs percentiles responds to changes in the contributing factors.

Leave-one-out cross-validation for prediction

A multiple linear regression model was developed to predict the peak value, POS, and EOS, incorporating various onset characteristics of flash flourishing growth. These include the start and end dates of the onset, the duration between these dates, the SIF or VIs values at both the onset's start and end, and the average SIF or VIs during the onset period. The model is represented by the following equations:

$$\mathrm{Peak} = a_1 \mathrm{Index}_{\mathrm{OB}} + a_2 \mathrm{Index}_{\mathrm{OE}} + a_3 \mathrm{Index}_{\mathrm{avg}} + a_0 \tag{4}$$

$$\mathrm{POS} = b_1 \mathrm{Date}_{\mathrm{OB}} + b_2 \mathrm{Date}_{\mathrm{OE}} + b_3 \mathrm{ONS}_{\mathrm{duration}} + b_0 \tag{5}$$

$$\mathrm{EOS} = c_1 \mathrm{Date}_{\mathrm{OB}} + c_2 \mathrm{Date}_{\mathrm{OE}} + c_3 \mathrm{ONS}_{\mathrm{duration}} + c_0 \tag{6}$$

In these equations, $a_0, a_1, a_2, a_3, b_0, b_1, b_2, b_3$, and c_0, c_1, c_2, c_3 represent the coefficients estimated through the multivariable regression procedure for the peak value, POS, and EOS, respectively. $\mathrm{Index}_{\mathrm{OB}}$ refers to the SIF or VIs values at the onset's beginning, $\mathrm{Index}_{\mathrm{OE}}$ to the values at the onset's end, $\mathrm{Index}_{\mathrm{avg}}$ to the average SIF or VIs value during the onset period. $\mathrm{Date}_{\mathrm{OB}}$ is the start date of the onset, $\mathrm{Date}_{\mathrm{OE}}$ is the end date, and $\mathrm{ONS}_{\mathrm{duration}}$ denotes the duration between the start and end of the onset.

To assess the model's predictive accuracy, a robust leave-one-out cross-validation (LOOCV) approach was applied. For instance, to predict the peak values for 2005, the regression coefficients were calculated using data from all years except 2005, specifically from 2003 to 2004 and 2006 to 2022. A similar process was followed for predicting 2006, where the model was trained using data from 2003 to 2005 and 2007 to 2022. This procedure was repeated for each year, generating annual predictions from 2003 to 2022. It is essential to note that the regression coefficients (a0, a1, a2, a3, etc.) differ each year due to the nature of the regression analysis. The dominant prediction factor for each year was identified as the one with the highest absolute regression coefficient. Across the period from 2003 to 2022, the dominant prediction factor was defined as the one with the highest frequency of the largest absolute regression coefficient.

The model's performance was assessed by examining the linear relationship between the predicted (sim) and observed (obs) values, and calculating the root mean square error (RMSE) using the following formula:

$$\mathrm{RMSE} = \sqrt{\frac{\sum_{\mathrm{i}=1}^{\mathrm{n}} (\mathrm{obs_i} - \mathrm{sim_i})^2}{\mathrm{n}}} \tag{7}$$

Where n is the total number of observations, and i denotes the index of individual observation.

Furthermore, predictability at each pixel was computed according to the Eq. (8):

$$Predictability = \left(1 - \frac{|obs - sim|}{obs}\right) \times 100\% \tag{8}$$

Higher values of predictability indicate a stronger agreement between simulated and observed values, and thus greater predictive skill.

Path analysis

We conducted path analysis within a structural equation modeling (SEM) framework to disentangle the direct and indirect influences of flash flourishing onset characteristics, phenological traits, and climatic drivers on peak greenness, POS, and EOS. All models were specified a priori and estimated in R (v. 4.3.3) using the lavaan package, which returns standardized path coefficients for each hypothesized causal link[63]. Indirect pathways were quantified as the product of standardized coefficients along successive legs of the model[64], thereby partitioning each predictor's total effect into its direct component and any mediated (e.g., climatic- or POS-driven) contributions. Model adequacy was assessed using standard SEM fit indices, including the chi-square statistic (χ^2), its degrees of freedom (df) and associated model-level p value, the chi-square-to-degrees-of-freedom ratio ($\frac{\chi 2}{df}$), and the goodness-of-fit index (GFI). Given the very large sample sizes in our models (n ≈ 10,000 per subsample), the χ^2 test and $\frac{\chi 2}{df}$ ratio are expected to be highly sensitive and almost always statistically significant, so we interpret model adequacy primarily in terms of the overall pattern of standardized path coefficients and GFI, rather than relying on χ^2 alone. The $\frac{\chi 2}{df}$, model-level p value, and GFI for all SEMs are reported in Supplementary Table S5 so that readers can evaluate model performance directly. To verify the stability of our estimates given the large sample, we performed ten independent bootstrapped subsamples ($n = 10{,}000$ each), reran the full SEM for each draw in R and confirmed that path coefficients and fit metrics remained similar across all replicates.

Data availability

This study investigated rapid vegetation growth in NEL from 2003 to 2022 using five remote sensing datasets focused on solar-induced fluorescence (SIF) and vegetation indices (VIs) (Supplementary Table S1). The continuous SIF (CSIF) dataset (https://osf.io/8xqy6/), a globally harmonized spatiotemporal product generated through machine learning, was utilized. This dataset integrates raw SIF observations from the Orbiting Carbon Observatory 2 (OCO-2) with predictor variables derived from the MCD43C1 C6 reflectance product[65]. In addition to SIF, the PKU GIMMS NDVI dataset was employed, which combines data from the Advanced Very High Resolution Radiometer (AVHRR) and the Moderate-Resolution Imaging Spectroradiometer (MODIS)[6] (Li et al. [66]). To further investigate vegetation dynamics, Enhanced Vegetation Index (EVI) and kernel Normalized Difference Vegetation Index (kNDVI) data were sourced from the MODIS MOD13C1 version 6 product. EVI data were directly retrieved, while the kNDVI was calculated based on the MOD13C1v6 NDVI dataset[50]. Gap-filled leaf area index (LAI) data from the MODIS C6 product were also included in the analysis (http://globalchange.bnu.edu.cn/research/laiv6). Additionally, we analyzed simulated 19 gross primary productivity (GPP) and 12 LAI datasets generated by process-based ecosystem models within the TRENDY v12 framework (Supplementary Tables S2, S3). These models are built upon core biogeochemical and physiological principles, capturing key processes such as photosynthesis, respiration, carbon allocation in vegetation, and soil biogeochemistry (https://blogs.exeter.ac.uk/trendy/). They simulate the response of these processes to environmental drivers, including temperature, soil moisture, atmospheric CO_2 levels, and land-use and land-cover change (LULCC). The TRENDY models utilize atmosphere and CO_2 input fields derived from observational datasets[28], which serve as the basis for model simulations and evaluations. Each model runs under four experimental scenarios: S0 represents a control case with static environmental forcing, S1 introduces time-varying CO_2 while keeping other factors unchanged, S2 further incorporates temporal atmospheric variations while maintaining constant LULCC, and S3 accounts for dynamic changes in CO_2, atmosphere, and LULCC. By analyzing the differences between S1–S0, S2–S1, and S3–S2, the distinct impacts of CO_2, atmosphere variability, and LULCC on vegetation flash flourishing growth can be isolated[67]. To validate the analysis, gross primary productivity (GPP) data from the FLUXNET data product, including FLUXNET2015 and AmeriFLUX datasets (https://fluxnet.org/data/regional-network-data/), were analyzed. Sites selected for this analysis met the following criteria: (i) located in NEL (>30°N), (ii) a minimum observation period of 10 years, and (iii) evidence of at least one instance of vegetation flash flourishing growth events. Based on these criteria, 44 sites were selected from the FLUXNET dataset, with detailed site information presented in Supplementary Table S4. Because the available site records extend from 2003 to 2021, we have defined this interval as the focal period for our FLUXNET GPP analysis. Environmental factors influencing vegetation flash flourishing growth were assessed using temperature (TMP), precipitation (PRE), and radiation (RAD) data from the CRU JRA v2.4 dataset (https://catalogue.ceda.ac.uk/uuid/aed8e269513f446fb1b5d2512bb387ad).
Vapor Pressure Deficit (VPD) was calculated from ERA5 2 m TMP and 2 m dew point temperature data (https://cds.climate.copernicus.eu/apps/user-apps/app-c3s-daily-era5-statistic), following the method described by Bolton[11]. Soil moisture (SM) data were sourced from the surface soil moisture dataset of the Global Land Evaporation Amsterdam Model (GLEAMv4.1a)[68]. We used CRU JRA v2.4 temperature directly as the TMP predictor, while ERA5 temperature is only employed together with ERA5 dew point to derive a physically consistent VPD field. Thus, temperature and VPD are treated as distinct predictors derived from separate, internally consistent datasets, rather than mixing temperature from two sources within the same variable. Using the MODIS landcover dataset (MCD12C1v6, type 3), we categorized the vegetation in NEL into three types: grasslands, shrublands, and forests[67] (comprising savannas, evergreen broadleaf forests, deciduous broadleaf forests, evergreen needleleaf forests, and deciduous needleleaf forests) (https://lpdaac.usgs.gov/products/mcd12c1v006/) (Supplementary Fig. S5). To ensure consistency across datasets, all satellite-based data were resampled to a spatial resolution of 1/12° × 1/12°, allowing for precise calculations of each flash growth event. Similarly, the TRENDY-simulated data were resampled to a coarser resolution of 1/2° × 1/2°. The study area in NEL (>30°N) was defined based on two criteria: NDVI values exceeding 0.125 and an irrigation coverage fraction of 10% or less (Data were collected around 2005; http://www.

fao.org/aquastat/en/geospatial-information/global-maps-irrigated-areas/latest-version/). Additionally, cropland areas identified using the MCD12C1v6 dataset (land cover type 3) were excluded from the analysis to focus on non-agricultural ecosystems.

Received: 14 October 2025; Accepted: 25 January 2026;

References

1. Hong, S. et al. Contrasting temperature effects on the velocity of early- versus late-stage vegetation green-up in the Northern Hemisphere. *Glob. Chang. Biol.* **28**, 6961–6972 (2022).
2. Yao, J. et al. Impact of shifts in vegetation phenology on the carbon balance of a semiarid sagebrush ecosystem. *Remote Sens.* **14**, 5924 (2022).
3. Boulton, C. A., Ritchie, P. D. L. & Lenton, T. M. Abrupt changes in Great Britain vegetation carbon projected under climate change. *Glob. Chang. Biol.* **26**, 4436–4448 (2020).
4. Denham, S. O. et al. The rate of canopy development modulates the link between the timing of spring leaf emergence and summer moisture. *J. Geophys. Res. Biogeosci*. **128**, e2022JG007217 (2023).
5. Lian, X. et al. Diminishing carryover benefits of earlier spring vegetation growth. *Nat. Ecol. Evol.* **8**, 218–228 (2024).
6. Li, Y. et al. Widespread spring phenology effects on drought recovery of Northern Hemisphere ecosystems. *Nat. Clim. Chang.* **13**, 182–188 (2023).
7. Kim, J. H., Sohn, S., Wang, Z. & Kim, Y. Nonuniform response of vegetation phenology to daytime and nighttime warming in urban areas. *Commun. Earth Environ*. **5**, 308 (2024).
8. Wu, X. et al. Canopy structure regulates autumn phenology by mediating the microclimate in temperate forests. *Nat. Clim. Chang*. **14**, 1299–1305 (2024).
9. Buitenwerf, R., Rose, L. & Higgins, S. I. Three decades of multi-dimensional change in global leaf phenology. *Nat. Clim. Chang.* **5**, 364–368 (2015).
10. Shen, M. et al. Challenges in remote sensing of vegetation phenology. *Innov. Geosci.* **2**, 100070 (2024).
11. Zeng, L., Wardlow, B. D., Xiang, D., Hu, S. & Li, D. A review of vegetation phenological metrics extraction using time-series, multispectral satellite data. *Remote Sens. Environ.* **237**, 111511 (2020).
12. Park, H., Jeong, S. & Peñuelas, J. Accelerated rate of vegetation green-up related to warming at northern high latitudes. *Glob. Chang. Biol.* **26**, 6190–6202 (2020).
13. Liu, Z. et al. Enhanced vegetation productivity driven primarily by rate not duration of carbon uptake. *Nat. Clim. Chang*. https://doi.org/10.1038/s41558-025-02311-3 (2025).
14. Chen, M. et al. Rapid growth of Moso bamboo (Phyllostachys edulis): cellular roadmaps, transcriptome dynamics, and environmental factors. *Plant Cell* **34**, 3577–3610 (2022).
15. Jiang, N., Shen, M. & Yang, Z. Differential phenological responses to temperature among various stages of spring vegetation green-up. *J. Plant Ecol.* **17**, rtae063 (2024).
16. Koolen, S. P. et al. The coexistence of trees, shrubs, and grasses creates a complex picture of land surface phenology in dry tropical ecosystems. *Remote Sens.* **17**, 2883 (2025).
17. Toomey, M. et al. Greenness indices from digital cameras predict the timing and seasonal dynamics of canopy-scale photosynthesis. *Ecol. Appl.* **25**, http://ameriflux.ornl.gov/ (2015).
18. Kay, B. D., Hajabbasi, M. A., Ying, J. & Tollenaar, M. Optimum versus non-limiting water contents for root growth, biomass accumulation, gas exchange and the rate of development of maize (Zea mays L.). *Soil Tillage Res.* **88**, 42–54 (2006).
19. Wang, Y. et al. Increasing optimum temperature of vegetation activity over the past four decades. *Earths Fut.* **12**, e2024EF004489 (2024).
20. Lian, X. et al. Summer soil drying exacerbated by earlier spring greening of northern vegetation. *Sci. Adv.* **6**, eaax0255 (2020).
21. Zhang, Y., Keenan, T. F. & Zhou, S. Exacerbated drought impacts on global ecosystems due to structural overshoot. *Nat. Ecol. Evol.* **5**, 1490–1498 (2021).
22. Chapin, F. S., Matson, P. A., Mooney, H. A. & Vitousek, P. M. Principles of terrestrial ecosystem ecology. New York, NY: Springer NewYork. (2002).
23. Mao, J. et al. Human-induced greening of the northern extratropical land surface. *Nat. Clim. Chang.* **6**, 959–963 (2016).
24. Zhu, Z. et al. Greening of the Earth and its drivers. *Nat. Clim. Chang.* **6**, 791–795 (2016).
25. Getu Engida, T., Nigussie, T. A., Aneseyee, A. B. & Barnabas, J. Land use/land cover change impact on hydrological process in the Upper Baro Basin, Ethiopia. *Appl. Environ. Soil Sci*. **2021**, 6617541 (2021).
26. Winkler, K., Fuchs, R., Rounsevell, M. & Herold, M. Global land use changes are four times greater than previously estimated. *Nat. Commun*. **12**, 2501 (2021).
27. Higgins, S. I., Conradi, T. & Muhoko, E. Shifts in vegetation activity of terrestrial ecosystems attributable to climate trends. *Nat. Geosci.* **16**, 147–153 (2023).
28. Friedlingstein, P. et al. Global carbon budget 2022. *Earth Syst. Sci. Data* **14**, 4811–4900 (2022).
29. Fleischer, K. & Terrer, C. Estimates of soil nutrient limitation on the CO_2 fertilization effect for tropical vegetation. *Glob. Chang. Biol.* **28**, 6366–6369 (2022).
30. Reich, P. B., Hobbie, S. E. & Lee, T. D. Plant growth enhancement by elevated CO_2 eliminated by joint water and nitrogen limitation. *Nat. Geosci.* **7**, 920–924 (2014).
31. Oguchi, R. et al. An intraspecific negative correlation between the repair capacity of photoinhibition of cold acclimated plants and the habitat temperature. *Plant Cell Environ*. https://doi.org/10.1111/pce.15270 (2024).
32. McDermid, S. S. et al. Disentangling the regional climate impacts of competing vegetation responses to elevated atmospheric CO_2. *J. Geophys. Res. Atmos.* **126**, e2020JD034108 (2021).
33. Solovchenko, A. E. & Merzlyak, M. N. Screening of visible and UV radiation as a photoprotective mechanism in plants. *Russian J. Plant Physiol.* **55**, 719–737 (2008).
34. Rahmati, M. et al. Continuous increase in evaporative demand shortened the growing season of European ecosystems in the last decade. *Commun. Earth Environ*. **4**, 236 (2023).
35. Jiasen, W. et al. Eco-stoichiometric characteristics of carbon, nitrogen and phosphorus in leaves and soil of camellia oleifera at different age. *J. Southwest For. Univ.* **39**, 86–92 (2019).
36. Saini, K., Dwivedi, A. & Ranjan, A. High temperature restricts cell division and leaf size by coordination of PIF4 and TCP4 transcription factors. *Plant Physiol.* **190**, 2380–2397 (2022).
37. Tan, Y. et al. The role of reactive oxygen species in plant response to radiation. *Int. J. Mol. Sci.* **24**, https://doi.org/10.3390/ijms24043346 (2023).
38. Meng, F. et al. Consistent time allocation fraction to vegetation green-up versus senescence across northern ecosystems despite recent climate change. *Sci. Adv.* **10**, https://www.science.org (2024).
39. Wang, L. et al. The widely increasing sensitivity of vegetation productivity to phenology in northern middle and high latitudes. *Geophys. Res. Lett*. **52**, e2024GL113892 (2025).
40. Shi, S., Yang, P. & van der Tol, C. Spatial-temporal dynamics of land surface phenology over Africa for the period of 1982–2015. *Heliyon* **9**, e16413 (2023).
41. Qiao, Y. et al. Accelerating effects of growing-season warming on tree seasonal activities are progressively disappearing. *Curr. Biol.* **33**, 3625–3633.e3 (2023).

42. Liu, Z. et al. Increased early-season productivity drives earlier peak of vegetation photosynthesis across the Northern Hemisphere. *Commun. Earth Environ*. **6**, 157 (2025).
43. Shi, S., Yang, P., Vrieling, A. & Tol, C. van der. Vegetation optimal temperature modulates global vegetation season onset shifts in response to warming climate. *Commun. Earth Environ.* **6**, 203 (2025).
44. Xu, X., Riley, W. J., Koven, C. D. & Jia, G. Observed and simulated sensitivities of spring greenup to preseason climate in Northern Temperate and Boreal Regions. *J. Geophys. Res. Biogeosci.* **123**, 60–78 (2018).
45. Ganguly, S., Friedl, M. A., Tan, B., Zhang, X. & Verma, M. Land surface phenology from MODIS: characterization of the collection 5 global land cover dynamics product. *Remote Sens. Environ.* **114**, 1805–1816 (2010).
46. Zhang, X. et al. Monitoring vegetation phenology using MODIS. *Remote Sens. Environ.* **84**, 471–475 (2003).
47. Piao, S. et al. Plant phenology and global climate change: current progresses and challenges. *Global Change Biol.* **25**, 1922–1940 (2019).
48. Sun, Z. et al. Enhanced isoprene emission capacity and altered light responsiveness in aspen grown under elevated atmospheric CO2 concentration. *Glob. Chang. Biol.* **18**, 3423–3440 (2012).
49. Richardson, A. D. et al. Terrestrial biosphere models need better representation of vegetation phenology: results from the North American Carbon Program Site Synthesis. *Glob. Chang. Biol.* **18**, 566–584 (2012).
50. Mughal, N. et al. Adaptive roles of cytokinins in enhancing plant resilience and yield against environmental stressors. *Chemosphere* **364**, 143189 (2024).
51. Cong, N. et al. Changes in satellite-derived spring vegetation green-up date and its linkage to climate in China from 1982 to 2010: a multimethod analysis. *Glob. Chang. Biol.* **19**, 881–891 (2013).
52. Yuan, X. et al. Anthropogenic shift towards higher risk of flash drought over China. *Nat. Commun*. **10**, 4661 (2019).
53. Jamal, P., Ali, M., Faraj, R. H., Ali, P. J. M. & Faraj, R. H. 1-6 Data Normalization and Standardization: A Technical Report. Machine Learning Technical Reports 1 https://docs.google.com/document/d/1x0A1nUz1WWtMCZb5oVzF0SVMY7a_58KQulqQVT8LaVA/edit# (2014).
54. Piao, S., Fang, J., Zhou, L., Ciais, P. & Zhu, B. Variations in satellite-derived phenology in China's temperate vegetation. *Glob. Chang. Biol.* **12**, 672–685 (2006).
55. Chen, A., Meng, F., Mao, J., Ricciuto, D. & Knapp, A. K. Photosynthesis phenology, as defined by solar-induced chlorophyll fluorescence, is overestimated by vegetation indices in the extratropical Northern Hemisphere. *Agric. For. Meteorol*. **323**, 109027 (2022).
56. Ji, S. et al. Diverse responses of spring phenology to preseason drought and warming under different biomes in the North China Plain. *Sci. Total Environ.* **766**, 144437 (2021).
57. Abdi, H. Partial least squares regression and projection on latent structure regression (PLS Regression). *Wiley Interdiscip. Rev. Comput. Stat.* **2**, 97–106 (2010).
58. Rustam, F. et al. COVID-19 future forecasting using supervised machine learning models. *IEEE Access* **8**, 101489–101499 (2020).
59. Zhang, Y. et al. Earth's record-high greenness and its attributions in 2020. *Remote Sens. Environ*. **316**, 114494 (2025).
60. Zhou, Z. H. & Feng, J. Deep forest. *Natl. Sci. Rev.* **6**, 74–86 (2019).
61. Feng, Q. et al. Long-term gridded land evapotranspiration reconstruction using Deep Forest with high generalizability. *Sci. Data* **10**, 908 (2023).
62. Lundberg, S. M., Allen, P. G. & Lee, S.-I. A Unified Approach to Interpreting Model Predictions. https://github.com/slundberg/shap (2017).
63. Rosseel, Y. Journal of Statistical Software Lavaan: An R Package for Structural Equation Modeling. http://www.jstatsoft.org/ (2017).
64. Liu, Y. et al. Drought legacies delay spring green-up in northern ecosystems. *Nat. Clim. Chang*. https://doi.org/10.1038/s41558-025-02273-6 (2025).
65. Zhang, Y., Joiner, J., Hamed Alemohammad, S., Zhou, S. & Gentine, P. A global spatially contiguous solar-induced fluorescence (CSIF) dataset using neural networks. *Biogeosciences* **15**, 5779–5800 (2018).
66. Li, M. et al. Spatiotemporally consistent global dataset of the GIMMS Normalized Difference Vegetation Index (PKU GIMMS NDVI) from 1982 to 2022. *Earth Syst. Sci. Data* **15**, 4181–4203 (2023).
67. Kong, X. et al. Exploring the environmental drivers of vegetation seasonality changes in the northern extratropical latitudes: a quantitative analysis. *Environ. Res. Lett.* **18**, 094071 (2023).
68. Martens, B. et al. GLEAM v3: Satellite-based land evaporation and root-zone soil moisture. *Geosci. Model Dev.* **10**, 1903–1925 (2017).

Acknowledgements

J.M. would like to thank Xiaoman Lu for helpful discussions. H.C. and X.K. were supported by the National Key Research and Development Program of China (2022YFF0801603). X.K. was supported by the Postgraduate Research and Practice Innovation Program of Jiangsu Province (KYCX24_1414). J.M., Y.W., and X.S. were supported by the Oak Ridge National Laboratory (ORNL) through the Reducing Uncertainties in Biogeochemical Interactions through Synthesis and Computing Scientific Focus Area and the Terrestrial Ecosystem Science Scientific Focus Area, funded by the Earth and Environmental Systems Sciences Division of the Biological and Environmental Research Office within the U.S. Department of Energy Office of Science. ORNL is managed by UT-Battelle, LLC, for the DOE under contract DE-AC05-00OR22725.

Author contributions

J.M. conceived the study. X.K., J.M., H.C. wrote the manuscript. Z.Z., Y.H., Y.W., Y.Z., A.C., M.J., X.S., F.H. contributed to the framework of the manuscript and participated in the writing process. All authors have read and approved the final manuscript.

Competing interests

Author A.C. is an associate editor of the npj Climate and Atmospheric Science. A.C. was not involved in the journal's review of, or decisions related to, this manuscript. This manuscript has been authored by UT-Battelle, LLC, under contract DE-AC05-00OR22725 with the US Department of Energy (DOE). The US government retains, and the publisher, by accepting the article for publication, acknowledges that the US government retains, a nonexclusive, paid-up, irrevocable, worldwide license to publish or reproduce the published form of this manuscript, or allow others to do so, for US government purposes. DOE will provide public access to these results of federally sponsored research in accordance with the DOE Public Access Plan. The other authors declare no competing financial or non-financial interests.

Additional information

Supplementary information The online version contains supplementary material available at https://doi.org/10.1038/s41612-026-01346-3.

Correspondence and requests for materials should be addressed to Jiafu Mao or Haishan Chen.